Stochastic study of the temperature response of the upper ocean to uncertainties in the atmospheric forcing in an Atlantic OGCM

Marc A. Lucas, Nadia Ayoub, Bernard Barnier, Thierry Penduff, Pierre de Mey-Frémaux

▶ **To cite this version:**

Marc A. Lucas, Nadia Ayoub, Bernard Barnier, Thierry Penduff, Pierre de Mey-Frémaux. Stochastic study of the temperature response of the upper ocean to uncertainties in the atmospheric forcing in an Atlantic OGCM. Ocean Modelling, 2008, 20 (1), pp.90-113. 10.1016/j.ocemod.2007.07.006 . hal-00266974

HAL Id: hal-00266974
https://hal.science/hal-00266974

Submitted on 13 Feb 2020

HAL is a multi-disciplinary open access archive for the deposit and dissemination of scientific research documents, whether they are published or not. The documents may come from teaching and research institutions in France or abroad, or from public or private research centers.

L'archive ouverte pluridisciplinaire **HAL**, est destinée au dépôt et à la diffusion de documents scientifiques de niveau recherche, publiés ou non, émanant des établissements d'enseignement et de recherche français ou étrangers, des laboratoires publics ou privés.

Stochastic study of the temperature response of the upper ocean to uncertainties in the atmospheric forcing in an Atlantic OGCM

Marc A. Lucas [a,*], Nadia Ayoub [b], Bernard Barnier [c], Thierry Penduff [c], Pierre de Mey [b]

[a] *CNRM/GMGEC/EAC Meteo France, 42 Avenue Gaspard Coriolis, 31057 Toulouse, France*
[b] *LEGOS, 14 avenue Edouard Belin, 31400 Toulouse, France*
[c] *Equipe Meom, LEGI, BP53, 38041 Grenoble Cedex 9, France*

The impact of errors in atmospheric forcing on the behaviour of ocean models is a fundamental issue for ocean modellers and data assimilation and one that has yet to be fully addressed. In this study, we use a stochastic modelling approach with 50 7-months (September–March) primitive equation eddy permitting (1/4°) integrations. We investigate the response of the oceanic circulation to atmospheric uncertainties, focusing principally on their impact on the upper oceanic temperature field. The ensemble is generated by perturbing the wind, atmospheric temperature and incoming solar radiation of the ERA40 reanalysis. Each perturbation consists of a random combination of the 20 dominant EOFs of the difference between the ERA40 and NCEP/CORE reanalysis datasets. The ensemble standard deviation of various interfacial and oceanic quantities is then examined in the upper 200 m of three distinct regions of the North Atlantic: in the Gulf Stream, in the Northern Tropical band and in the North East Atlantic. These show that even a very small perturbation of the atmospheric variables can lead to significant changes in the ocean properties and that regions of oceanic mesoscale activity are the most sensitive. The ocean response is driven by vertical diffusivity and eddy activity. The role of subsurface currents is also crucial in carrying the eddy signal away from the regions of mesoscale activity. Finally, the decorrelation time scale of the mesoscale activity is critical in determining the amplitude of the oceanic response.

Keywords: Stochastic modelling; Atmospheric perturbations; Heat content; North Atlantic

1. Introduction

The knowledge of the mechanisms governing the ocean heat content distribution and their response to atmospheric forcing is a key issue in understanding the ocean–atmosphere coupled system. It has been addressed in

* Corresponding author. Tel.: +33 5 61 07 99 12.
E-mail address: marc.lucas@cnrm.meteo.fr (M.A. Lucas).

many different studies and a lot of understanding about upper ocean processes has been gained (e.g. Rudnick and Ferrari, 1999; Ferrari and Bocaletti, 2004). Among these studies, many are based on modelling, from conceptual models to high resolution Ocean General Circulation Models (e.g. Noh et al., 2002; Boccaletti et al., 2005; Caniaux and Planton, 1998). This has involved considerable effort in improving the parameterisation of upper ocean processes, such as vertical mixing. Simultaneously, a new generation of atmospheric products, with improved realism and space–time sampling, have been made available to force OGCMs, as for instance, ECMWF and NCEP reanalyses and datasets derived from satellite observations. The parallel efforts on OGCMs on the one hand and atmospheric forcing products on the other raise another question that is fundamental, but that has received little attention: what is the response for a given model to errors in the atmospheric forcing, in particular in terms of representation of upper ocean heat content? In this paper, we aim to address this issue, in the specific case of an eddy-permitting simulation of the North Atlantic circulation.

The difficulty in dealing with such an issue stems from three main reasons. The first one is the complexity of the physical processes involved (i.e. those governing the model response to the atmospheric forcing itself) and the wide range of space and time scales associated: from the large scales of the ocean circulation to the turbulent sub-meter scales. The second reason is linked to the nature of the errors or uncertainties in the atmospheric forcing: errors in the air–sea exchange formulation (e.g. bulk formulae) or in the atmospheric forcing fields themselves. Most OGCMs are forced with numerical weather prediction (NWP) products such as ECMWF or NCEP (re)analyses. Uncertainties in these products arise from errors in NWP models, in data assimilation schemes and in the assimilated observations, as well as from the scarcity of observations in some regions. Unfortunately, the error estimations are usually not provided with the fields and remain poorly known. The third difficulty is more methodological: how can we estimate a model response (or 'model errors') to errors in parameters or boundary conditions, such as errors in the atmospheric forcing?

Estimates of model errors are necessary for the evaluation of the degree of realism of the simulations as well as for a better interpretation of model–data misfits. In particular, data assimilation or state estimation methods require the specification of model errors. The latter are given as the covariance matrix of forecast errors or background errors on the control variables. Model errors are usually unknown (or incompletely known); their estimates are often based on strong assumptions of stationarity and homogeneity. Stochastic modelling offers the possibility to quantitatively estimate the model response to given perturbations on state variables, parameters and boundary/initial conditions. It constitutes the basis of the so-called Ensemble Kalman Filter (Evensen, 2003), where the forecast error covariance matrices are computed from statistics on an ensemble of simulations (as an approximation of the dynamical Fokker–Planck equation) and are updated by the filter. The estimation of errors in OGCMs, including the identification of their space–time structures, is an issue which has not really been addressed yet, in all likelihood because of complexity of the problem and of numerical computation limitations. Recently, it has received more attention in particular through the use of stochastic modelling (see among recent studies: Wirth and Ghil, 2000; Auclair et al., 2003). When data are assimilated, a posteriori comparisons between forecast and analysis may allow one to 'adjust' the a priori error covariance estimate (so-called 'adaptive methods'). In the context of ocean/weather forecasting, statistical tests are developed to check the forecast against a priori assumptions and first guess error covariances, leading possibly to the rejection of a priori estimates. However, these methods are not aimed at providing a systematic discussion of the errors spatial and temporal structures. To our knowledge, there are very few attempts to analyze OGCM errors and interpret them in terms of physical processes; those that exist are essentially conducted with coastal models (Echevin et al., 2000; Auclair et al., 2003; Jordà-Sanchez, 2005) or short (daily) time scales in limited areas (e.g. Andreu-Burillo et al., 2002). In this work, we adopt such an approach but in the case of a basin-scale eddy-permitting simulation on longer time scales.

Our general objective is to explore the model response and the associated mechanisms to uncertainties in atmospheric fields in an eddy-permitting simulation of the North Atlantic at seasonal scales. We focus on the heat content representation in the upper layers. The period of study is September 1994–March 1995. Such a period has been chosen as it corresponds to the seasonal deepening of the mixed-layer: we thus expect the sensitivity of the upper ocean to the atmospheric signal to be high. We use an ensemble method which consists of building a set of perturbations for the atmospheric forcing, then generating an ensemble of simulations each driven by the different perturbed atmospheric fields. We characterize the model response from the ensemble statistics of the induced ocean perturbations. This paper presents the results for the temperature field only

and addresses the following issues: what is the impact of atmospheric uncertainties on SST? How does it penetrate to depth? What are the time scales and physical processes associated? The impact on other surface variables and heat budgets as well as estimates of covariances will be examined in a forthcoming article.

The paper is organized as follows: the OGCM and atmospheric forcing fields are presented in the next section. In Section 3, we describe the atmospheric perturbations and the generation of the ensemble of simulations. In Section 4, the ensemble spreads of air–sea heat and momentum fluxes and of ocean temperature profiles are presented and we identify the principal mechanisms associated with the subsurface ocean response to the atmospheric perturbations. The main conclusions and their implications are discussed in Section 5.

2. Set up

2.1. Model

The model used in this study is based on the NEMO OGCM (Madec, 2006) a free-surface, z-coordinate, primitive equation code coupled to the LIM ice model (Goosse and Fichefet, 1999). The North Atlantic configuration used here belongs to the hierarchy of NEMO-based ocean model configurations developed by the DRAKKAR project. It is referred to as NATL4 and was built up as a regional extraction of the 1/4° global DRAKKAR configuration extensively described in Barnier et al. (2006), in particular in terms of its coastlines and bottom topography. Major characteristics of NATL4 are described in Le Sommer et al. (2006). They are only summarized here. The horizontal mesh is a 1/4° resolution tri-polar ORCA grid (see Barnier et al., 2006) which covers the Atlantic Ocean and the Nordic Seas from latitude 20°S to 80°N. The vertical grid has 46 geopotential levels with a grid spacing ranging from 6 m at the surface to 250 m for the lowermost level. The bottom topography is represented with partial steps (full steps were used in Le Sommer et al., 2006). Buffer zones are defined at the northern and southern boundaries and in the eastern Mediterranean Sea, inspired by the methodology used in the DYNAMO project (Willebrand et al., 2001) where temperature and salinity are relaxed to the climatological fields of Levitus et al. (1998). A Laplacian isopycnal mixing of tracers (coefficient of 300 m^2/s at the equator) as well as a bilaplacian diffusion of momentum (coefficient of 1.6×10^{11} m^4/s at the equator) are used in the lateral mixing parameterization. Both coefficients are decreasing toward the pole as the first and third power of the grid step, respectively. Vertical physics are parameterized by a 1.5 order closure model, the Turbulent Kinetic Energy or TKE scheme (Blanke and Delecluse, 1993), to which an enhanced vertical mixing of tracers and momentum is added in case of static instability. In this model configuration, the background diffusion (Kz) is set to 10^{-5} m^2/s. In the surface layers, the TKE vertical mixing scheme allows the diffusion coefficient to vary between 10^{-4} and 1 m/s (very exceptionally above 1). When static instabilities occur, Kz is increased to 10 m^2/s. Quadratic bottom friction and free slip lateral boundary conditions are used. There is no restoring to surface climatological values for the salinity or the temperature and the river run-offs are parameterised using a monthly data set.

2.2. Forcing

Forcing fields used in this study are from the ERA40 reanalysis provided by the ECMWF (Uppala et al., 2005). They consist in six hourly winds at a height of 10 m, humidity and temperature at 10 m, daily incoming solar radiation and outgoing long wave radiation, daily rain and snowfall. Precipitation fields have been corrected following Troccoli and Kallberg (2004). The atmospheric variables are first interpolated on the model grid and then used to drive the model. The model does its calculation of the surface fluxes every 5 h using the bulk formulae proposed by Large and Yeager (2004), the above variables from ERA40 and its own diagnostic sea surface temperature.

2.3. Reference run

The model starts on January 1st 1987, from rest and from the climatological values of Levitus et al. (1998) for temperature and salinity. The model spin-up lasts 7 years and 8 months and uses the ERA40 interannual reanalysis fields; the period of study for the ensemble simulations spans from September 1994 to March 1995.

A reference experiment, i.e. without any perturbations added to the forcing, is run from September 1994 to December 1997. A full description of the reference run is beyond the scope of this paper and we just present here the main features of the mean temperature (T) and salinity (S) distribution at the surface. A more detailed presentation will be given in a future paper. The 3-year average of T and S fields is calculated over 1995–1997 and compared to the Levitus et al. (1998) climatology. The differences in sea surface temperature (SST) are minor, less than 1.5 °C over most of the basin. They reach slightly higher values in upwelling areas along the African coasts, where neither the model nor the atmospheric forcing have a sufficient resolution to properly represent the upwelling physics. The misfits are larger (~3 °C) in the Labrador basin and along the Greenland coasts; they are maximum (~8 °C) in the Gulf Stream region. These important differences are down to the issue of boundary current separation point which is too northerly in the model. For the sea surface salinity, the difference with the climatology falls between −0.75 and 0.75 PSU over most of the basin except in wintertime ice covered regions and near river outflows where it increases significantly (up to 8 PSU, not shown). Runoff estimates is a critical issue locally for short time scales and globally at annual time scales (recall there is no restoring to climatological values at surface). In the rest of our study, we will focus on areas far from rivers outflows.

3. Experimental strategy

3.1. A priori uncertainties on ERA40 fields

The first step of our work consists in generating a set of perturbations on the ERA40 forcing fields over the period September 1994–March 1995. The perturbed variables are the air temperature, the zonal and meridional wind velocities and the incoming solar flux. By perturbing these variables, we induce perturbations on all the air–sea fluxes components: momentum, heat and fresh water. Recall that our objective is to explore the ocean model's response to uncertainties in the atmospheric forcing; therefore, the perturbations should represent uncertainties on the ERA40 variables. The question now is: what are the uncertainties on ERA40 fields? They are not provided by the reanalysis and there is no estimate available over the whole basin and period of the experiment. In this study, we choose to represent the ERA40 uncertainties by the differences between ERA40 fields and their equivalent in the CORE products of Large and Yeager (2004). This is a choice among others, motivated by the fact that ERA40 and CORE datasets have similar space–time sampling and coverage. Such a strategy is also used by Leeuwenburgh (2005) in a data assimilation study in the Tropical Pacific; his motivations and the detailed method to generate the perturbations are however different from ours. CORE fields are derived from the NCEP/NCAR reanalysis (Kalnay et al., 1996) for the air temperature and wind velocity and from satellite observations for the radiative fluxes (ISCCP, Zhang et al., 2004). These fields have then been adjusted by Large and Yeager (2004) based on comparisons with in situ or satellite datasets. In terms of data frequency, CORE winds and air temperature are given every 6 h and incoming solar radiation every 12 h, as they are in the ERA40 dataset.

It is clear that by this approach, i.e. estimating the a priori uncertainties on ERA40 fields from the differences between ERA40 and CORE datasets, the errors estimates do not represent the full range of errors in the ERA40 variables. This is mainly because both ECMWF and NCEP NWP models are based on similar physical assumptions and also because common observations are used in both assimilation systems and as boundary conditions. As a result, the main features of the large scale atmospheric circulation and variability are expected to be similarly represented in the two reanalyses. The 'errors' defined by the differences between ERA40 and CORE are the signature of: (1) the differences between the ECMWF and NCEP atmospheric models (physical parameterisations, numerical schemes), (2) the differences between the data assimilation systems and (3) the adjustments made by Large and Yeager (2004) on the original NCEP/NCAR reanalysis to create the CORE product. However, the differences in terms of radiative fluxes have a different nature since, in the CORE dataset, they come from satellite observations. It is beyond the scope of this paper to describe extensively the differences observed between the atmospheric variables from CORE and ERA40. Briefly, the wind module variations are fairly well correlated between both datasets but the amplitude of the CORE winds is greater than that of the ERA40 ones. Little differences are found on air temperature whereas large

discrepancies are observed for the downward radiation on both time variability and mean values: ERA40 fluxes are stronger at high latitudes and weaker in the tropical band (Brodeau et al., 2006).

3.2. Generation of the perturbations on ERA40 fields

The perturbations on ERA40 variables are built by first calculating the differences between the ERA40 (s_{ERA40}) and CORE (s_{CORE}) six hourly fields without the climatology having been removed, where s represents air temperature (T10), incoming solar flux (Qsol) and the meridional (V10) and zonal (U10) wind velocities. We then compute the EOFs of the differences over the study period (September 1994–March 1995):

$$\underbrace{s_{\mathrm{ERA40}}(x,y,t) - s_{\mathrm{CORE}}(x,y,t)}_{s} = \delta s_{\mathrm{mean}}(x,y) + \sum_i \theta_i(t)\psi_i(x,y) \tag{1}$$

where θ_i is the amplitude of the time series of the EOF number i, Ψ_i, and $\delta S_{\mathrm{mean}}(x,y)$ is the temporal mean of the difference over September 1994–March 1995.

Differences between ERA40 and CORE in U10, V10 and T10 are likely to be correlated because of the dynamical link between these variables. In order to account for the correlation, we compute multivariate EOFs for U10, V10 and T10. Differences in Qsol are deemed independent from those in U10, V10 and T10 as, in the CORE dataset, Qsol is derived from satellite data and not from the NCEP reanalysis model. Hence a second set of (univariate) EOFs for Qsol is calculated over the period September 1994–March 1995. The first multivariate EOF represents roughly 9% of the signal. In order to represent at least 50% of the variability, it is necessary to take the dominant 20 multivariate EOFs, which add up to 51% of the variability. For the univariate solar radiation EOFs, these numbers are, respectively, 15% and 53%.

The perturbations on the ERA variable (s_{ERA40}) are then based on a random combination of the dominant EOFs. More precisely, for each members' of the perturbations ensemble, the dominant 20 EOFs multiplied by a random number are added to (s_{ERA40}). In order to insure that the ensemble average of the perturbations has a zero mean at every time step, we generate pairs of perturbed fields built from the same perturbation but with an opposite sign. The kth perturbed field (s'_k) writes as follows:

$$s'_k(x,y,t) = s_{\mathrm{ERA40}}(x,y,t) + \sum_{i=1}^{20} \alpha_i^k \theta_i(t)\psi_i(x,y) \tag{2}$$

α_i^k is a random number from a normal distribution with a zero bias and unit standard deviation for the ith EOF mode and the kth perturbation.

We choose not to include in our a priori errors on ERA40, based on the differences between ERA40 and CORE fields, the time mean of these differences. This choice was made in order to keep the perturbed fields close to the ERA40 ones rather than defining a kind of 'mixed' ERA40-CORE forcing set. This means that we consider that the a priori uncertainties of the ERA40 variables are unbiased over the period of study. This is a relatively strong assumption that could be relaxed in further experiments testing different kind of atmospheric forcing errors. Note however that, by construction, the time mean of our perturbations over the period of study is not equal to zero since we do not retain all the EOF modes and since each mode is multiplied by a different random number (α_i^k).

In this setup, the coefficients α_i^k are taken as constant over the period of study. Other choices could have been made (like seasonally varying coefficients), adding some 'randomness' in the perturbations. But the objective here is to build perturbations whose temporal correlation is given by the EOFs amplitude time series for each mode, so the coefficients α_i^k have to be constant. Besides, for each variable, (U10, V10, T10, Qsol) the ratio between the variability of the signal built by adding the 20 dominant EOFs (with all α_i^k equal to one) and the variability of the ERA40 variable over the period of study is, on average over the basin, less than 5%. So in order, to build perturbations with a non negligible amplitude with respect to the (non-perturbed) ERA40 variable, we chose to accept relatively high values (>1) for the random coefficients α_i^k by generating them from a normal distribution with unit variance. The resulting amplitude of the perturbations is discussed in Section 4.1.

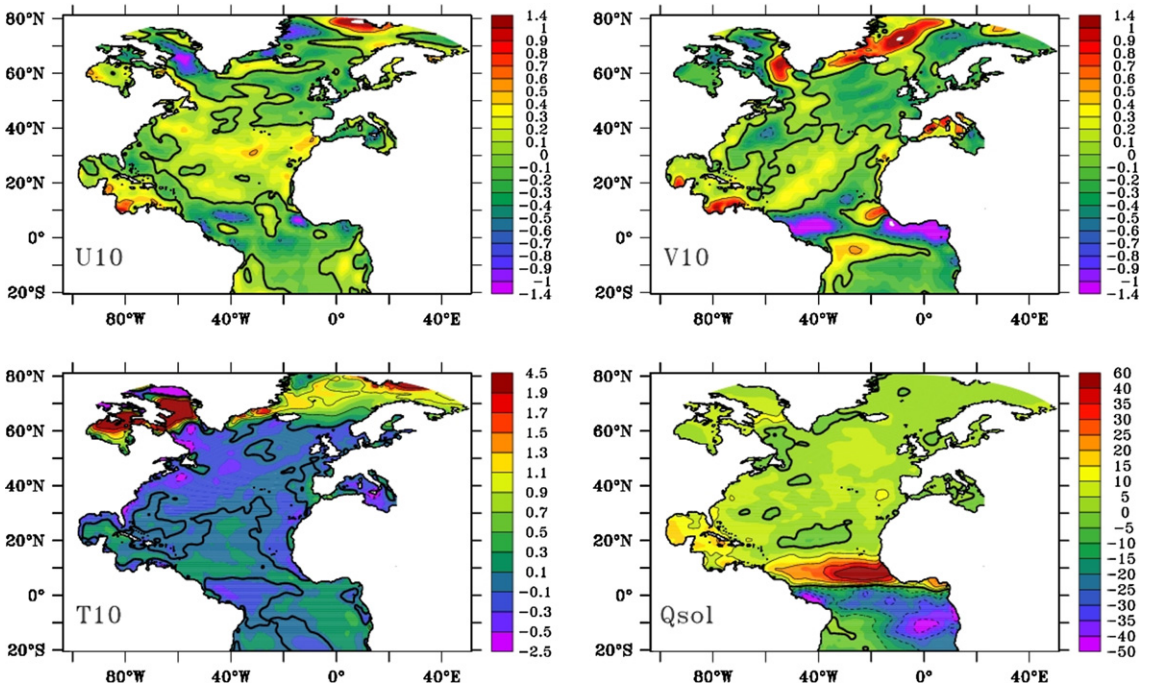

Fig. 1. Spatial pattern of the first EOFs in U10, V10, T10 and Qsol. Contour intervals are 0.5 m/s for U10 and V10, 0.5 °C for T10 and 10 W/m^2 for Qsol. Thick line indicates 0 value, dashed line indicates negative values.

In terms of the spatial distribution (Fig. 1), the first EOFs for the meridional and zonal winds U10 and V10 show roughly a tripolar pattern, wind variations in the tropics and subpolar gyre being in phase, and in opposing phase with wind variations in the subtropical gyre. Beside this large scale characteristic, smaller specific patterns are seen in the Labrador and Greenland Seas, in the area of the Gulf Stream separation for example. The amplitude is fairly small. The first atmospheric temperature EOF identifies the 60°N line as the axis of a bi-modal variability pattern, temperature changes being out of phase on each side of this line. The solar flux EOF, with an axis of phase change along the equator reflects the dominance of the annual cycle. In terms of temporal variability, the first two EOFs have high frequency fluctuations superimposed on a season-like oscillation (Fig. 2). The higher EOFs mode time series predominantly display high frequency variability. It is interesting to note that the time series for both univariate and multivariate EOFs have virtually identical season-like cycles for the first two modes.

3.3. Generation of the ensemble of simulations

Each member k of the ensemble is run over the period September 1994–March 1995, starting from the same initial conditions obtained from the spin-up over the period January 1987–September 1994. The model is then forced by a perturbed field (s'_k). In terms of data output, each run provides an estimate of surface fluxes and ocean variables evolution over the 7 month period. Five days averages are stored. In our study, the ensemble size is limited to 50 members, due to the computational cost of each run. We are aware that a greater number of members would increase the relevance of the statistics (variance, covariance). We have checked that no fundamental changes are obtained on the ensemble spread in temperature when using 30, 40 or 50 members (see Section 4.3). We therefore expect that in terms of space–time structure and underlying physical processes, an ensemble with a few tens of additional members would not behave in a significantly different way and the main results and conclusions drawn in this paper would remain unchanged.

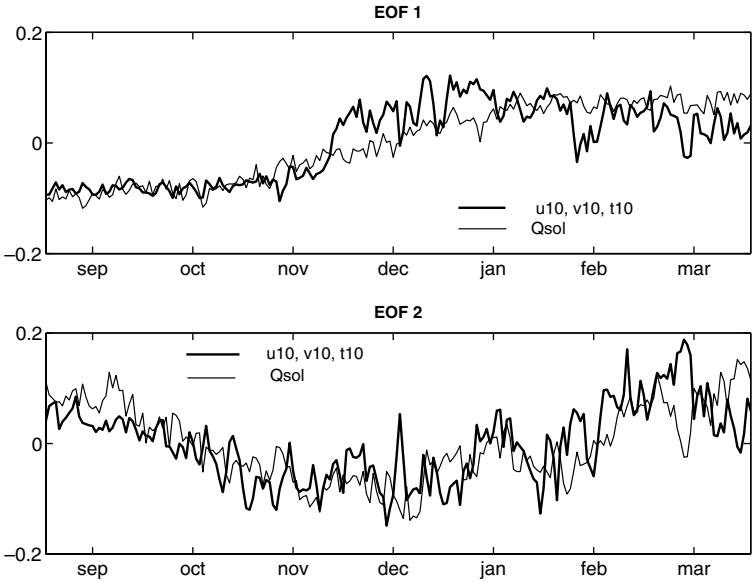

Fig. 2. Amplitude of the time series of EOFs 1 (top panel) and 2 (bottom panel), in thick line for the multivariate EOFs and thin line for the Qsol EOFs.

4. Results

4.1. General basin-scale features and definition of the three main zones of interest

Our analysis is based on the ensemble spread at a given date for every quantity which is calculated by computing the standard deviation over the ensemble with respect to the ensemble mean. As shown in Fig. 3a and b, the areas of maximum ensemble spread are the most dynamic ones, i.e. the Gulf Stream and the North Atlantic current, the Labrador Sea boundary current as well as the equatorial region. At the surface, in frontal regions such as south of Newfoundland, the ensemble spread has an amplitude of about 10% of the natural variability, that is the standard deviation over the study period of the temperature in the reference run (Fig. 3c and e). Further upstream in the western boundary current (just off the coast of America), outside the frontal region, this fraction increases to over 50% (Fig. 3e). In the tropical regions, the ensemble spread reaches a maximum of over 50% of the natural variability (Fig. 3e). Significant ensemble spread values are also observed in the subsurface. At 100 m, (panels b, d and f), in most of the Gulf Stream sector, they reach 40–50% of that of the natural variability. In the tropical regions however, at 100 m, the ensemble spread is swamped by the seasonal signal though it still represents about 10% of the natural variability just off the coast of Brazil (Fig. 3f). An ensemble spread of significant amplitude is still present at great depth (0.7 °C at 1000 m) in the Gulf Stream sector (not shown). Generally, the surface spread is greater than that at depth but this is not always the case: for instance, on the western side of the basin, between 0°N and 10°N, the maximum ensemble spread occurs at 100 m. The detailed patterns and the amplitude of the ensemble standard deviation evolve with time and the maps of Fig. 3 would be different if taken at another date of the experiment. However, the areas of maximum and minimum of the ensemble spread remain the same over the period of study. The spatial structure of the ensemble spread displays much smaller scales than the natural variability, at all depths. This analysis shows that the oceanic perturbations resulting from the artificial atmospheric perturbations used in this study are significant in view of their ratio with the natural variability.

In the following sections, we focus our study on three regions characterized by different magnitudes and space–time structures in the ocean response, namely the North East Atlantic (region NEATL), the North Tropical area (region TROP) and the Gulf Stream area (region GS). The regions are shown on Fig. 3a and correspond to boxes of 50 by 50 grid cells (i.e. roughly 13.6° × 12.6°). Most quantities are spatially averaged

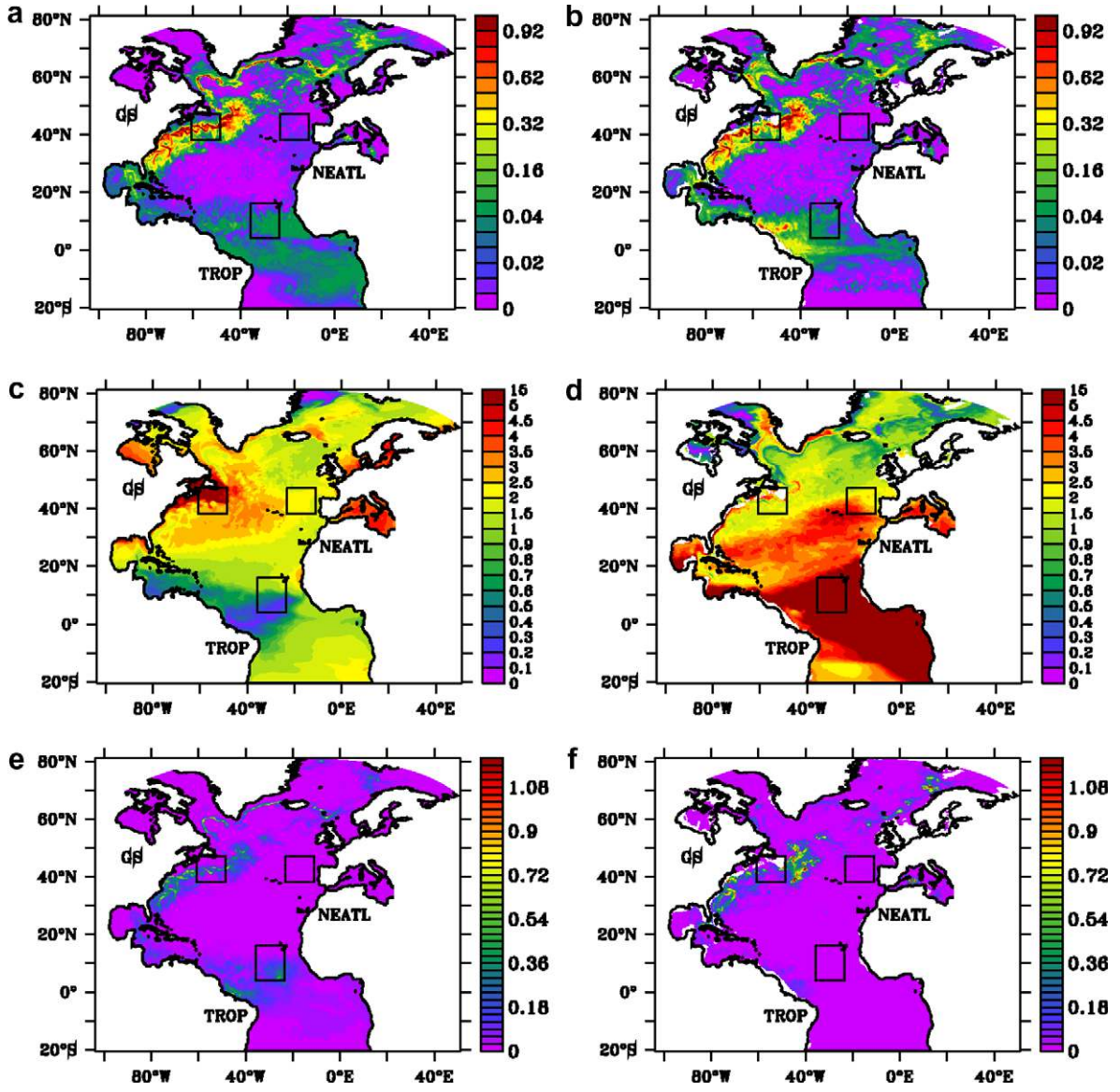

Fig. 3. Ensemble standard deviation of the temperature at the surface (panel a) and at 100 m (panel b), at the end of the experiment (29/03/1995). Natural standard deviation over the study period at the surface (panel c) and at 100 m (panel d) and ratios of the two at the surface (panel e) and at 100 m (panel f). Values in all panels are in °C.

over each box in order to lessen the signature of short term eddy activity. This is particularly important in region GS which straddles the Gulf Stream. Our study is based on the analysis of the time evolution of the ensemble standard deviation and mean of the atmospheric and oceanic quantities averaged over the three boxes. There are three types of variables presented here: atmospheric state variables (which are those directly perturbed), air–sea fluxes and ocean only variables (which result from the ocean model integration). The air–sea fluxes response to the atmospheric perturbations is highly non-linear because of the non-linearity of the bulk formulae used and because of the oceanic feedback. It is thus important to analyse them prior to examining the ocean's response. In the rest of this study, we therefore make a distinction between the so-called atmospheric perturbations, i.e. the perturbations on the wind, incoming solar flux and air temperature; interface perturbations, i.e. perturbations of the wind stresses and heat flux; and the ocean perturbations, i.e. perturbations on ocean only quantities such as temperature and velocity.

4.2. Atmospheric perturbations and interface signal

In order to understand how the ocean responds to perturbations in the atmospheric signal, it is important to know what the ocean actually responds to, in other words, how the heat flux and wind stress are perturbed in response to the perturbations on the atmospheric forcing variables. We evaluate the perturbations amplitude and spatial scales relative to the unperturbed fields by examining maps of the ensemble mean standard deviation over time of the perturbations. We then compare these maps to the unperturbed field averaged over the same period and to its standard deviation over time (here referred to as the natural variability).

In region NEATL (Fig. 4), U10 and V10 (not shown) perturbations have a maximum amplitude of 10% of the natural variability. For T10, the perturbations represent less than 1% of the natural variability. In all cases, the spatial scales are smaller than that of the natural variability. The solar flux perturbations have slightly smaller spatial scales and are an order of magnitude smaller than the natural variability. The heat flux perturbations amplitude on the other hand reaches a maximum of about a third of the maximum natural variability (108 W/m^2) but is generally well below 10 W/m^2. The associated spatial scales are much smaller than those of the natural variability. The wind stress perturbations have the same spatial scales as the natural variability and are two orders of magnitude smaller.

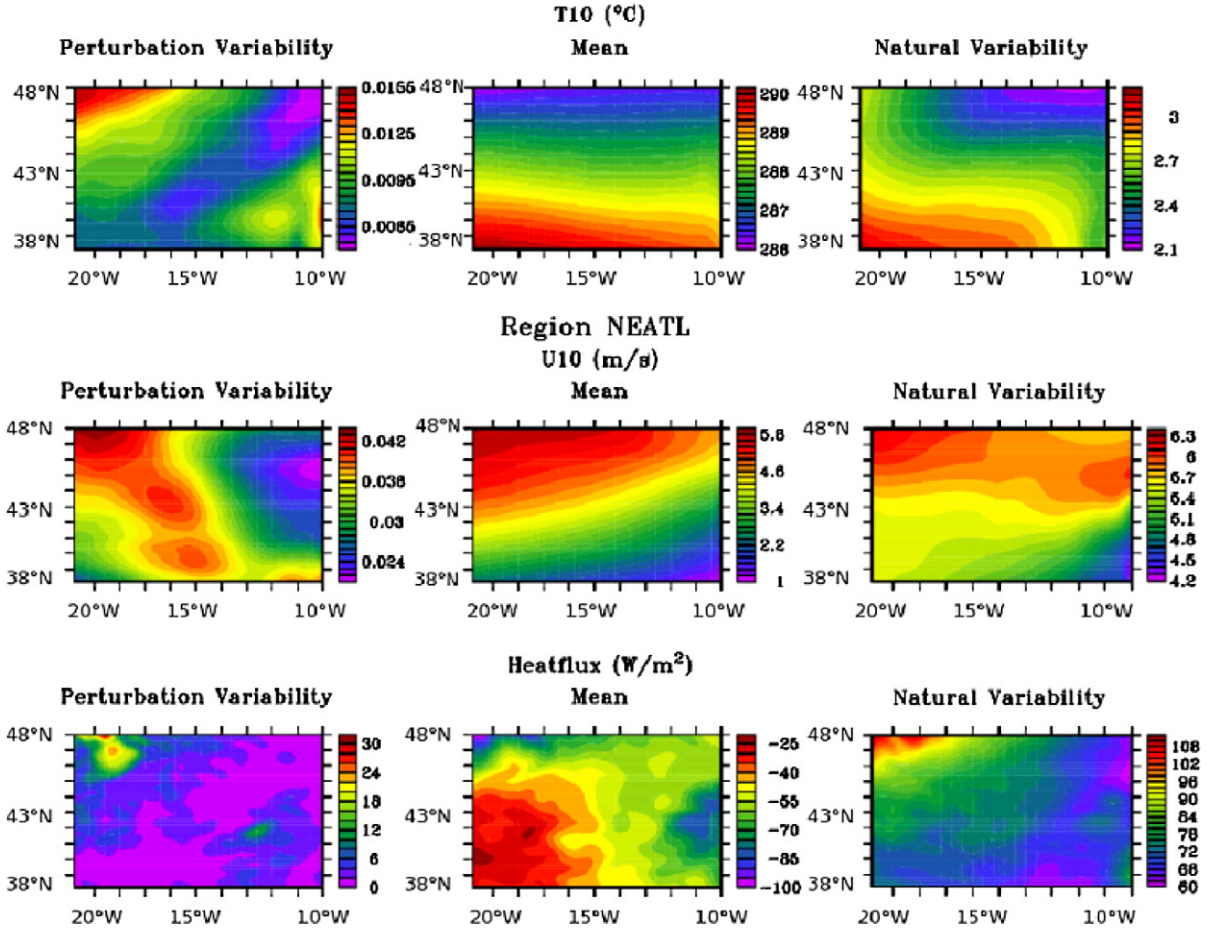

Fig. 4. Perturbation variability (mean ensemble standard deviation of the perturbation over the duration of the experiment) (left), natural variability (standard deviation of the reference field over the duration of the experiment) (right) and mean over the experiment (center) of T10 (up), U10 (middle) and Heat Flux (bottom) for region NEATL. The x-axis is in degrees of longitude and the y axis in degrees of latitude.

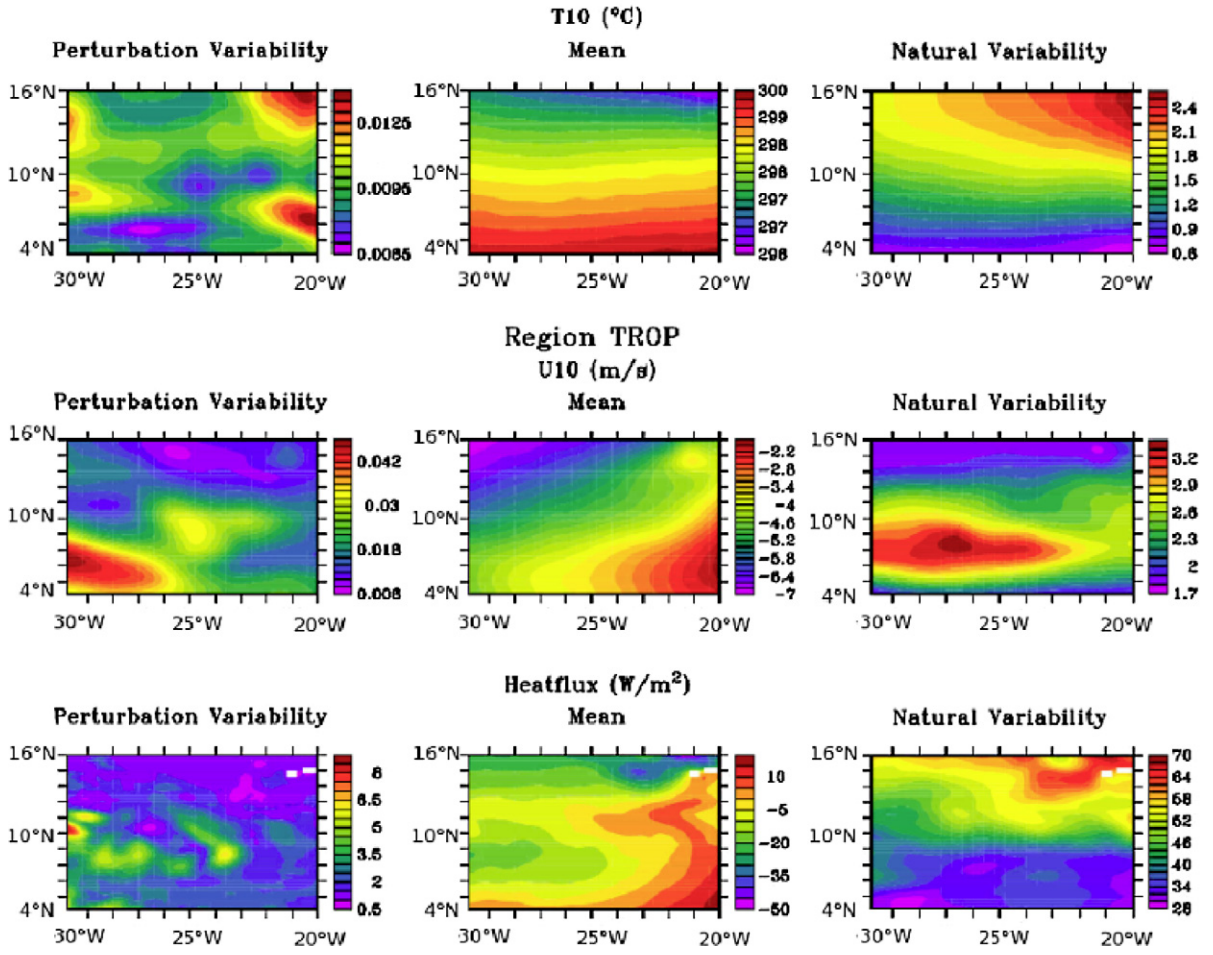

Fig. 5. Perturbation variability (mean ensemble standard deviation of the perturbation over the duration of the experiment) (left), natural variability (standard deviation of the reference field over the duration of the experiment) (right) and mean over the experiment (center) of T10 (up), U10 (middle) and heat flux (bottom) for region TROP. The x-axis is in degrees of longitude and the y axis in degrees of latitude.

In region TROP (Fig. 5), in terms of amplitude, the U10 and V10 perturbations also represent about 1% of the seasonal signal. T10 perturbations strength is about 0.6% of the natural variability. Spatially, they present patterns smaller than that of the natural variability, unlike the solar flux perturbations which are of the same spatial scales as that of the natural variability and an order of amplitude weaker. The heat flux perturbations maximum amplitude represents about 10% of the natural variability. The wind stress is an order of magnitude smaller and both have smaller spatial scales than the natural variability.

Finally, Fig. 6 shows clearly that, in region GS, in terms of amplitude, the atmospheric perturbations are very weak, reaching a maximum of 1% of the natural variability for U10 and V10, 0.6% for T10 and 6% for the incoming solar radiation. For all the variables, the perturbations have smaller spatial scales than those of the natural variability. At the interface, for the heat flux, the maximum amplitude is about 240 W/m^2, just above the 230 W/m^2 of the natural variability. The important role played by the ocean is obvious as the heat flux clearly shows the presence of a front and mesoscale signals not visible in the atmospheric variables but easily found in the SST (not shown). The response in the wind stress is much weaker, having smaller spatial scales and being an order of magnitude smaller than the natural variability.

Looking at the three regions and the amplitudes of the atmospheric signal, it is clear that the ocean plays a fundamental part in determining the heat flux response. For instance, the spread of the atmospheric perturbations in region GS is twice that of region NEATL but the resulting spread of heat flux perturbations is

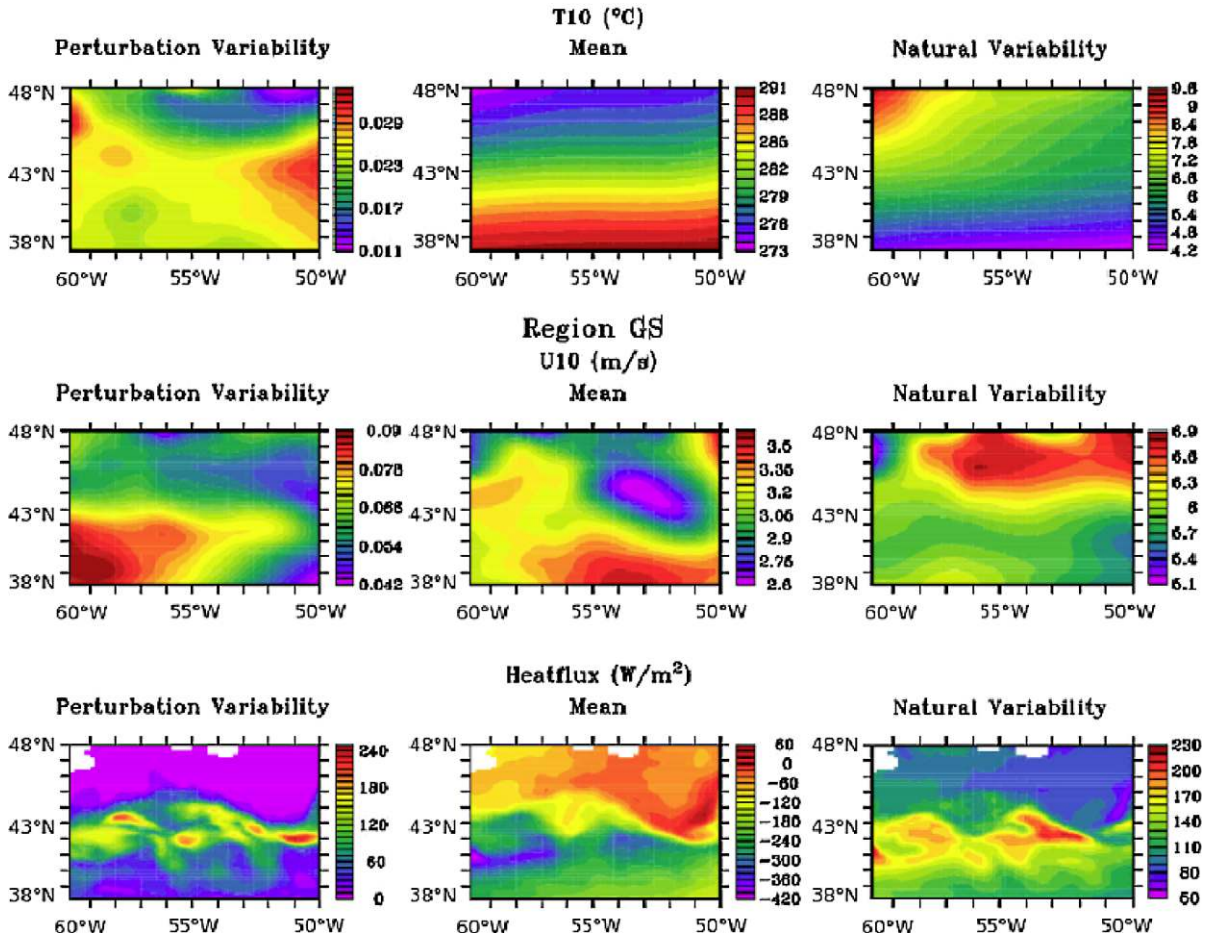

Fig. 6. Perturbation variability (mean ensemble standard deviation of the perturbation over the duration of the experiment) (left), natural variability (standard deviation of the reference field over the duration of the experiment) (right) and mean over the experiment (center) of T10 (up), U10 (middle) and heat flux (bottom), for the Gulf Stream region (region GS). The x-axis is in degrees of longitude and the y-axis in degrees of latitude.

almost ten times greater than for the heat flux perturbations in region NEATL. In effect, in region GS, the ocean appears to amplify the atmospheric signal, by up to an order of magnitude for the wind stress and even greater for the heat flux. It is striking that so weak differences in the atmospheric signal can lead to such big variations in fluxes, particularly bearing in mind that the bulk formulae are identical.

4.3. North East Atlantic region (region NEATL)

In Fig. 7, there appears to be no particular trend in the ensemble spread of the atmospheric quantities until November onwards where the spread of V10 and T10 slowly starts to increase (Fig 7a). There is also a hint of a seasonal cycle in the ensemble spread of the solar flux (Fig. 7b). In terms of mean values (not shown), there seems to be two distinct periods: one from September to December where the SST and Qsol show some agreement and a second one where none of the mean quantities appear correlated (not shown). This suggests a change of regime and could be linked to the deepening of the mixed layer depth (hereafter 'MLD') in the region. Generally, it seems that there is not one mechanism which is predominant in setting the SST in this region. This is not surprising in view of the fact that this region does not have strong ocean currents or any thermal fronts. It must be noted that the amplitudes of the perturbations in SST in region NEATL are an order of magnitude weaker than in region GS and TROP. At the interface, there seems to be a slow increase

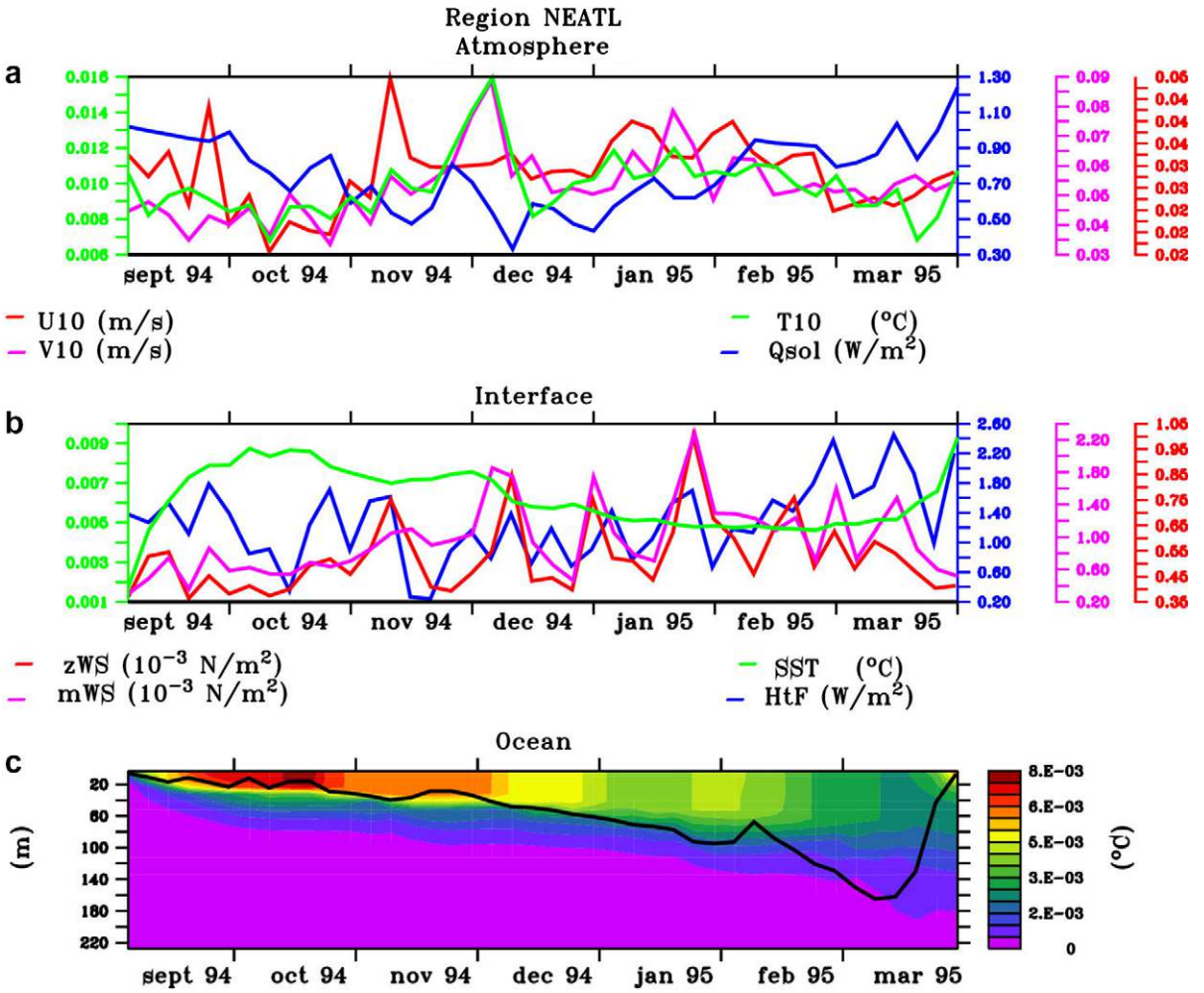

Fig. 7. Standard deviation on the ensemble of atmospheric variables (panel a), air–sea fluxes and SST (panel b), and ocean temperature in the North East Atlantic region (region NEATL) (panel c). The black curve on the lower panel is the mixed-layer depth (ensemble mean). For each variable, the mean is calculated over the box, then the standard deviation over the ensemble of the box mean is calculated.

in the ensemble spread of most of the quantities until the end of February. From March onwards, the wind stress ensemble spread decreases.

The structure of the oceanic temperature profile ensemble spread is fairly simple with the presence of two layers (Fig. 7c). In the upper 60 m, the spread initially increases until mid October before slowly decreasing until the end of March when it starts once again increasing. Below 60 m, the spread slowly increases throughout the experiment. The behaviour of the mean MLD (Fig. 7c) is fairly straight forward. It decreases by 150 m almost monotonically until mid March before rapidly increasing again, indicating a rapid restratification. The SST trajectories envelope (Fig. 8a) starts by slowly widening before shrinking slightly. The maximum width is only of about 0.03 °C. The ocean exhibits a fairly low sensitivity to the variations in the forcing as the envelope remains narrow. At 100 m (Fig. 8b), there is a monotonic increase in the width of the envelope, which reaches a width of 0.006 °C. There is very little similarity with what is observed at the surface suggesting that the local surface signal is greatly modified in the region as it propagates downwards and does not reach 100 m. As its amplitude at the surface is fairly small, this is not unexpected. The mixed layer heat content (MLHC) envelope grows virtually monotonically over time (Fig. 8c); it behaves more like the subsurface signal in Fig. 8b than the SST signal. The absence of mesoscale activity and strong currents in the region means that only the vertical diffusion carries the surface signal down beyond the depth at which convection occurs. There are two processes

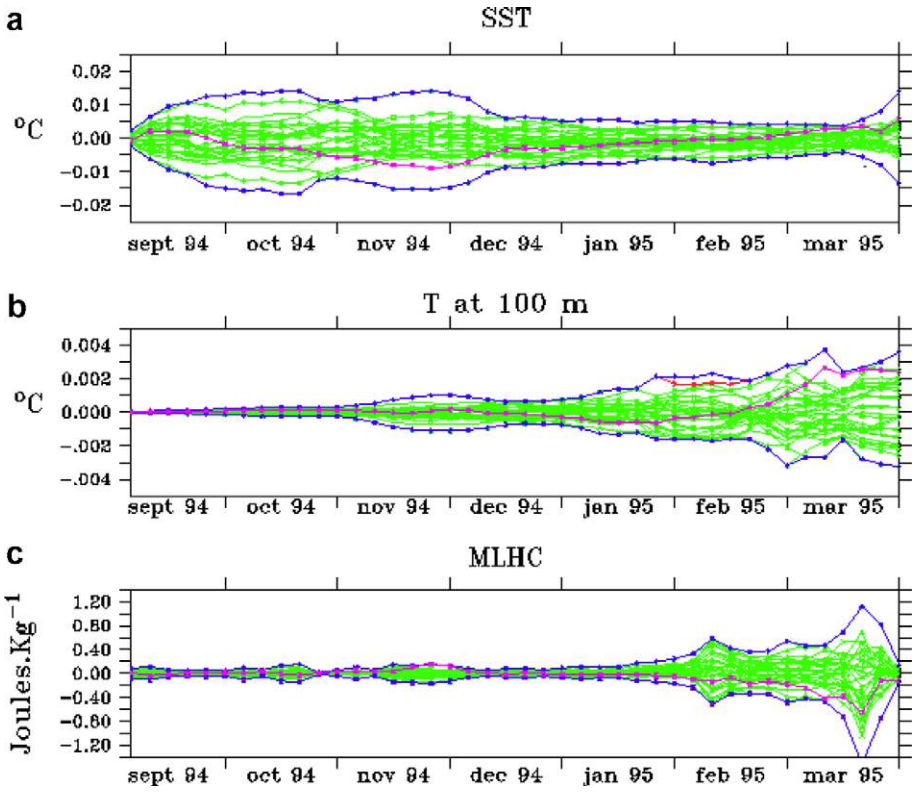

Fig. 8. Evolution as a function of time of the differences between each member's SST (panel a) temperature at 100 m (panel b) and mixed layer heat content (MLHC) (panel c) and the ensemble mean for region NEATL. The quantities are first averaged over the box before computing the difference with the ensemble mean. The green curves are the data for the each of the first 30 members, the red curve indicates the envelope for 40 members and the blue curve, the envelope for 50 members. These often overlay the red curves. The pink curve show the behaviour and variability of a single member.

at work: one which leads to an increase in the MLHC ensemble spread, the vertical transmission of the temperature ensemble spread and another one which both weakens and strengthens the signal, the deepening of the mixed layer. It leads to an increase in the Kz which means more of the mixed layer will be affected but more weakly as the perturbation is distributed over greater depths. Over the duration of the experiment, the depth of convection progressively increases until it encompasses the whole of the mixed layer. At this stage (mid February onwards), surface perturbations will impact on the whole mixed layer and as a result, the envelope of the heat content starts to widen. Similarly, the rapid shallowing of the mixed layer and convection towards the end of March leads to a drastic narrowing of the MLHC envelope that can be explained by two mechanisms. First, we observe that the shallowing of the mixed layer is accompanied by a reduction of the spread of its depth. Second, the MLHC is computed over a very thin layer which leads to more homogeneous values between the ensemble members.

Incidentally, it is interesting to note that the envelopes of the ensemble shown on the three panels of Fig. 8 are absolutely identical for 30, 40 and 50 members. This gives some confidence that the fundamental behaviour of the model has been adequately captured by the 50 member ensemble and that little would be gained by a computationally expensive increase in the size of the ensemble by a few tens of members.

In terms of transmitting the surface signal in the vertical, the vertical diffusion is the dominating mechanism. The high value in Fig. 9c results from the convective activity (note: we use 5-day averages outputs) that occurs there. In the first month or so, the SST ensemble spread in region NEATL increases in direct response to the atmospheric ensemble spread (Fig. 7c). This signal penetrates fairly rapidly to about 30 m because of the relatively high near surface Kz (Fig. 9c). It then weakens from November onwards because the mixed layer is deeper and the ensemble spread is thus rapidly propagated to greater depth (50 m). At the end of the

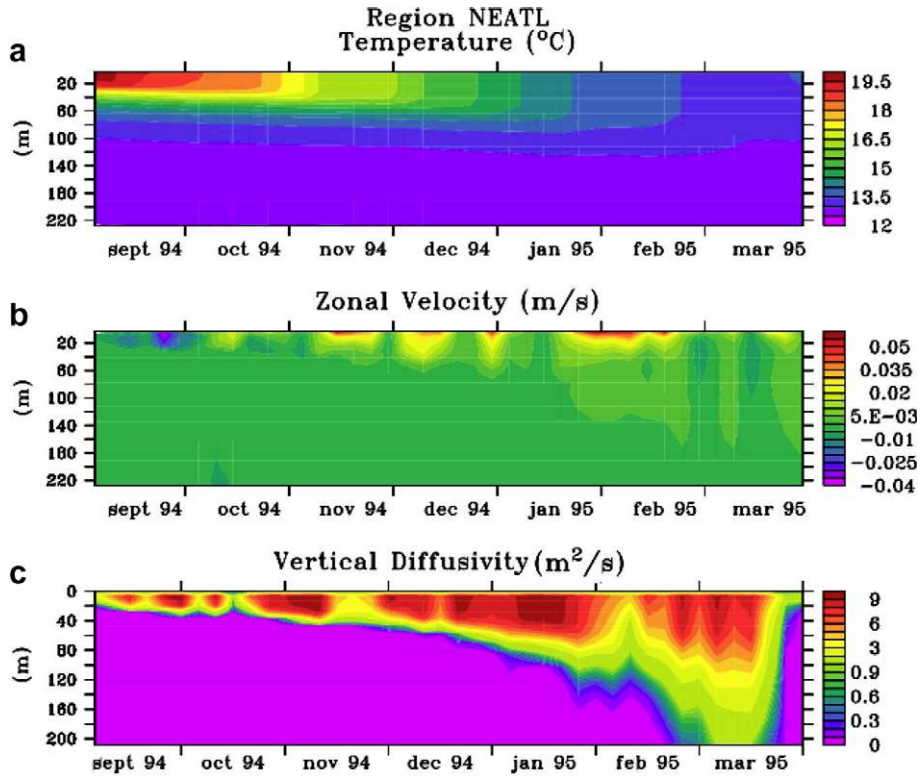

Fig. 9. Evolution as a function of time and depth of the ensemble mean temperature (°C) (panel a), mean zonal velocity (m/s) (panel b) and mean vertical diffusivity (m^2/s) (panel c) averaged over region NEATL.

experiment, the surface ensemble spread increases again predominantly because the MLD has shallowed significantly, and hence the signal does not penetrate further than the upper 20 m. This increases its intensity. Underlying this relatively rapid behaviour is the transmission of the ensemble spread in deeper layers with a weaker Kz. The surface signal reaches 180 m after about 7 months, at the end of the experiment.

4.4. North tropical region (region TROP)

In Fig. 10, the relation between the various variables appears fairly complex in region TROP. There is no discernible trend in most of the atmospheric quantities (Fig. 10a), except for the solar flux which shows a signal akin to a seasonal cycle (with a minimum in December and maxima in September and March). There seems to be some similarities in the trends of the standard deviation of heat flux and that of Qsol (Fig. 10b), but these two quantities have a behaviour which differs from that of the standard deviation of the SST. The obvious conclusion is that the ensemble spread of heat flux in this region predominantly comes from the perturbation of the solar flux, and not the SST, which indicates a weak sensible heat flux component. There is also some agreement between the mean winds and the mean heat flux which suggests a predominant role of the wind in controlling the heat flux in equatorial regions through the latent component (not shown). The lack of agreement between the behaviour of heat flux and that of the SST points towards an important role of advection in that region.

Looking at the ocean temperature profile spread, as in region NEATL (Fig. 10c), we have evidence of two regions. The upper 60 m show an increase until November followed by a decrease until January. From then on, the spread increases once again. Beneath this layer, we have a mid-depth maximum around 100 m which reaches its maximum value in January. This suggests that the ensemble spread at this depth is not just the result of the propagation of the local surface ensemble spread, particularly as there is a clear decoupling of

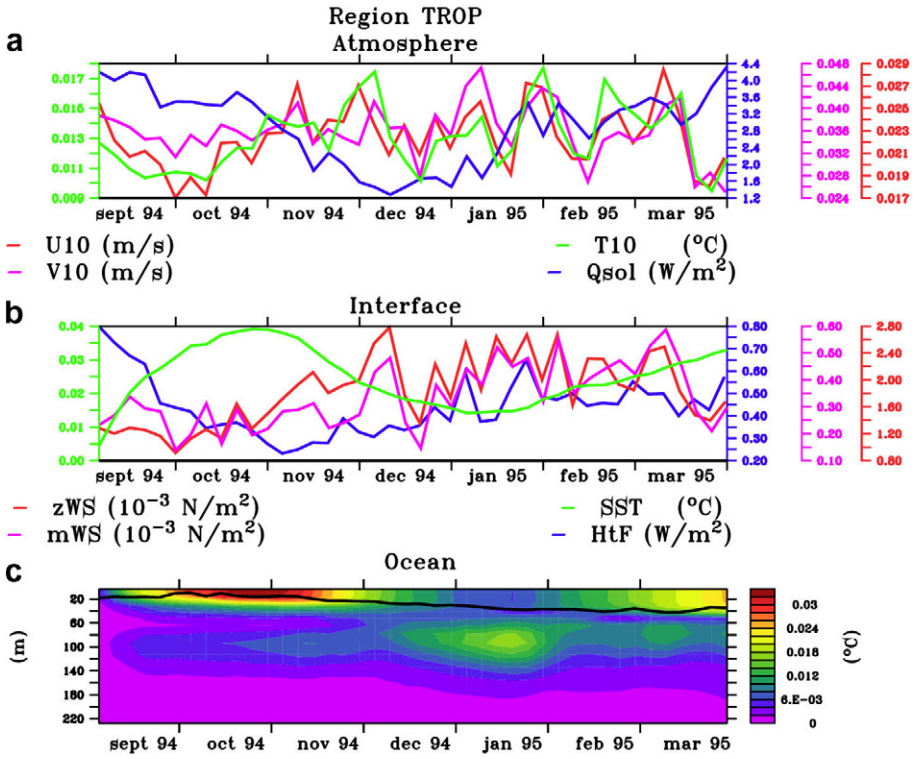

Fig. 10. Standard deviation on the ensemble of atmospheric variables (panel a), air–sea fluxes and SST (panel b), and ocean temperature in the Tropical region (region TROP) (panel c). The black curve on the lower panel is the mixed-layer depth (ensemble mean). For each variable, the mean is calculated over the box, then the standard deviation over the ensemble of the box mean is calculated.

the surface and deeper waters. Furthermore, the evolution of the ensemble spread of temperature appears cyclic in both the upper (decrease followed by an increase) and lower ocean (increase followed by a decrease). Regarding the behaviour of the MLD, we observe that the increase in region TROP is by far the smallest, with the mixed layer going from a depth of 24–48 m. There is little evidence of a shallowing towards the end of the experiment, although the depth has stabilised and is no longer increasing. The envelope of the SST trajectories (Fig. 11a) widens during the first 2 months then shrinks until the end of December before once again widening, albeit at a slower rate. Here, the maximum width is roughly 0.17 °C. The increase and decrease are monotonic. This would suggest that the spatial and temporal structures of the perturbations in the region have a large persistent spatial signal but this is not bourn out by the analysis of the heat flux and wind stress. At 100 m (Fig. 11b), the behaviour is similar to what happens at the surface, with a widening followed by a narrowing although there is a lag of about 4 months and the various features are not so pronounced. This latter aspect stems from the fact that the atmospheric signal has been dampened by other processes, namely advection. The range is fairly small, reaching a maximum of 0.05 °C in January. In terms of the MLHC (Fig. 11c), the picture is slightly more complex. The width of the envelope decreases then increases again. The slow rate of mixed layer deepening would in theory lend more weight to the surface layer processes and their vertical propagation. As a result, one could expect the behaviour of the mixed-layer heat content to be similar to that of the SST. The dominant mechanism however is the depth of the mixed layer. Initially, the MLHC spread decreases because of the decrease in the spread of the MLD (not shown). As can be seen in Fig. 12b, this decrease is followed by a period of weak advection and weak spread in the Qsol (Fig. 10b). This leads to a homogenization of the surface waters which are slowly being mixed with deeper waters (40–60 m), whose temperature spread is smaller (Fig. 10c). The subsequent increase corresponds to an increase in the MLD spread and the switch to the Ekman regime which brings waters with a higher surface temperature spread (see below).

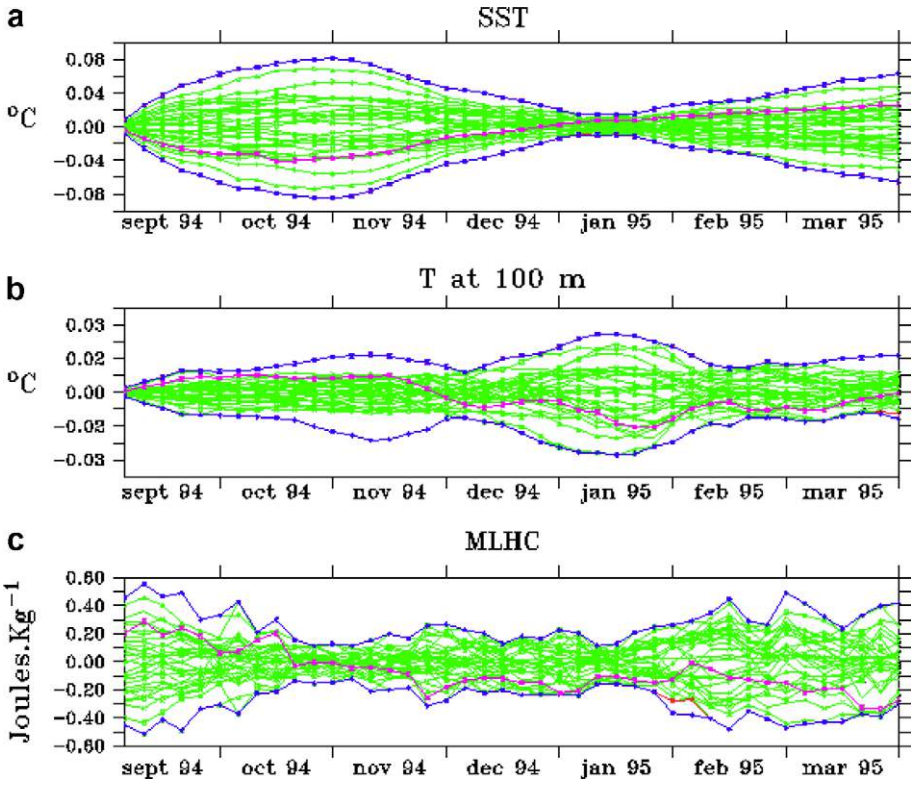

Fig. 11. Evolution as a function of time of the differences between each member's SST (panel a) temperature at 100 m (panel b) and mixed layer heat content (MLHC) (panel c) and the ensemble mean for region TROP. The quantities are first averaged over the box before computing the difference with the ensemble mean. The green curves are the data for the each of the first 30 members, the red curve indicates the envelope for 40 members and the blue curve, the envelope for 50 members. These often overlay the red curves. The pink curve show the behaviour and variability of a single member.

The upper waters of region TROP (down to ~60 m) are dominated by the zonal currents which undergo a reversal in late January–early February, as can be clearly seen in Fig. 12b. Until February, the zonal velocity is positive, indicating an eastward flowing current, the North Equatorial Counter Current (NECC, Stramma and Schott, 1996). From February onwards, a shallower westward flowing current is found, the northern branch of the South Equatorial Current (SEC), driven by the trade winds. These currents bring waters from regions which show greater sensitivity to the atmospheric perturbations than region TROP itself. In particular, the NECC brings in water from the North Brazil Current system which shows high sensitivity to the atmospheric perturbations. Similarly, the Ekman regime brings in cooler waters that originate off the coast of west Africa, a region of upwelling which also displays a high SST ensemble spread resulting from a high spread in the Qsol perturbations. As the vertical diffusion is enhanced (stronger Kz, see Fig. 12c), the surface signal propagates faster and deeper in March than for instance in October. The increase in Kz may be due to the cooler waters brought into the TROP region by the westward flow that create small instabilities leading to increased convective activity.

The mid depth waters display a type of signal that is absent from region NEATL, a region of weak advection. As mentioned earlier, this mid-depth signal is clearly decoupled from the local sub-surface signal, as is evident by the discontinuity in Fig. 10c. Two questions must be answered: first where does it come from and second how did it get to that depth (100 m or so) in view of the shallowness of the mixed layer (48 m maximum). The answer to the first question can be found by looking at the velocity distribution in the region. There is an eastward flowing current for most of the study period which extends from the surface down to about 130 m (Fig. 12b). From January onwards, this current starts to weaken, starting at the surface as it

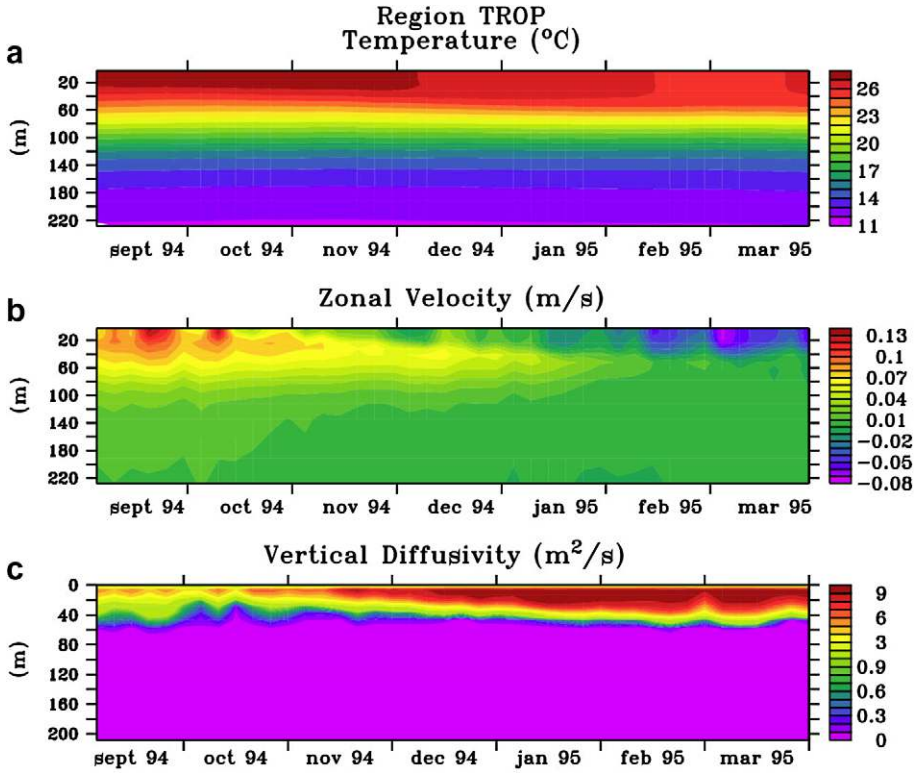

Fig. 12. Evolution as a function of time and depth of the ensemble mean temperature (°C) (panel a), mean zonal velocity (m/s) (panel b) and mean vertical diffusivity (m^2/s) (panel c) averaged over region TROP.

is gradually replaced by the northern branch of the SEC. To answer the second question, one needs to look in the region upstream of region TROP. There is some substantial mesoscale eddy activity (the Brazil Current rings) which form in summer and fall between 6 and 10°N. These eddies are generated by instabilities in the North Brazil Current, and have a signal that penetrates deep in to the ocean in excess of 100 m. Introducing small differences in the mean flow through perturbation in the forcing fields, notably the wind, leads to initially slight differences in the eddy field. These differences grow fairly slowly over time until January where because of the decorrelation of the mesoscale activity (discussed in greater detail later in Section 4.5), in under a month the ensemble spread at 100 m depth increases from 0.015 to 0.04 °C (not shown) with a fairly coherent vertical structure (in other words, in the region of the Brazil Current rings generation, the discontinuity found in region TROP at 40 m is not observed). These temperature perturbations are then advected by the eastward flowing North Equatorial Under Current (NEUC, Stramma and Schott, 1996) into region TROP. To summarise, in region TROP at depth, the temperature ensemble spread increases in January and decreases from early February onwards. The increase in the spread occurs because the mesoscale decorrelation time scale has been exceeded and therefore the waters brought in at depth by the eastward flowing current system (NECC/NEUC) have a strong temperature ensemble spread. The decrease occurs because of the weakening and eventual disappearance of the eastward current system. Note that the shallowness of the MLD throughout the experiment means that the MLHC is only affected by the surface currents (NECC, SEC), not the deeper NEUC and hence closely follows the behaviour of the SST (Fig. 11a).

4.5. Gulf Stream region (region GS)

In region GS, the spread of the atmospheric quantities does not display any outstanding trends throughout the study period (Fig. 13a). There is a simultaneous increase in the ensemble spread of the air temperature

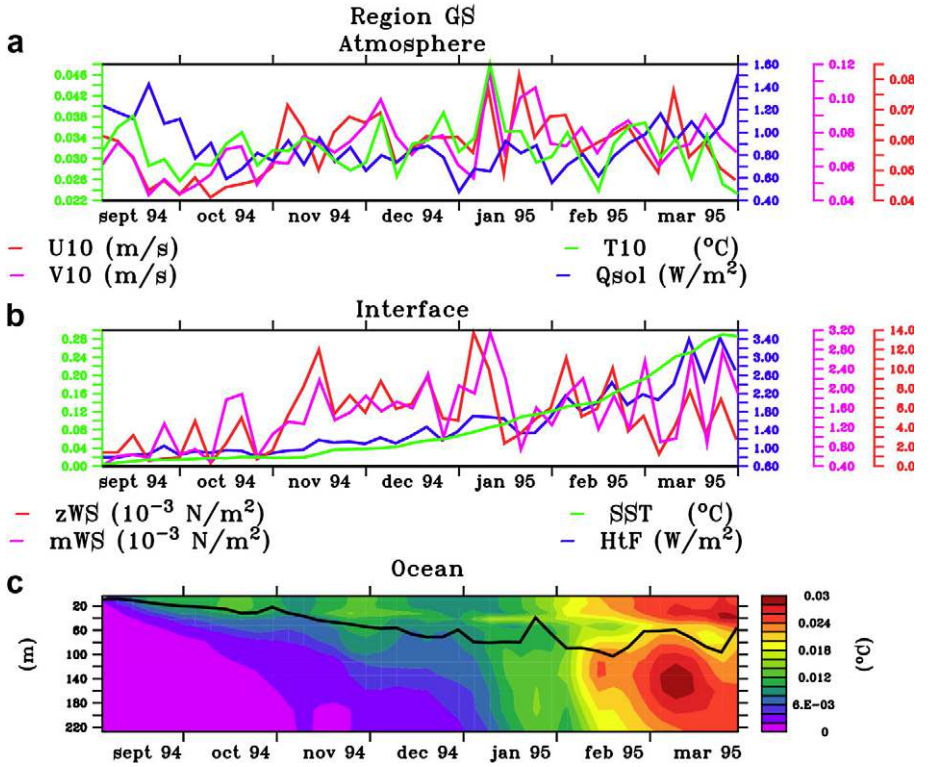

Fig. 13. Standard deviation on the ensemble of atmospheric variables (panel a), air–sea fluxes and SST (panel b), and ocean temperature in the Gulf Stream region (region GS) (panel c). The black curve on the lower panel is the mixed-layer depth (ensemble mean). For each variable, the mean is calculated over the box, then the standard deviation over the ensemble of the box mean is calculated.

(T10) and the winds (U10, V10) in January. In the interface, both wind stress components follow similar trends, with a marked increase in November. This increase occurs at the same period as the switch in the sign of the temporal series of the first EOF (Fig. 2). A striking aspect of Fig. 13b is the monotonic aspect of the standard deviations of the SST and the heat flux which grow over time. This is mirrored by the virtually monotonic seasonal decrease in the mean SST and sea surface height (not shown). It is difficult to clearly establish the succession of events: does reducing the SST simultaneously increase its ensemble spread and that of the heat flux? In any case, this close agreement suggests that the ensemble spread of the heat flux is controlled by the SST feedback.

The ocean temperature profile spread is fairly complex (Fig. 13c). There is the suggestion of two distinct regions, one in the upper 40 m with small scale features that broadly shows an increase in the ensemble spread and one below which is characterized by a slow increase in ensemble spread until January. From then on, the increase is faster and a mid-depth maximum appears which reaches its maximum value in early March before decreasing. This clearly indicates that the deeper waters are not solely subjected to a linear propagation of the surface signal and that more complex mechanisms come into play. The possibility that the subsurface maximum is an artefact of a bi modal distribution of members can be discounted by looking at the maximum and minimum mixed-layer depth over the ensemble (not shown), which are both deeper than the temperature spread subsurface maximum of Fig. 13c. The mean MLD (Fig. 13c) decreases by about 80 m and starts to show substantial oscillations with shallowing episodes of about 40 m from January onwards which is also the period where the spread of SST and T100 (temperature at 100 m depth) trajectories increases markedly. The SST envelope (Fig. 14a) progressively widens over time albeit in a fairly irregular fashion. The width of the envelope reaches a maximum of about 0.1 °C. In this region, the small spatial scales dominate the forcing due to the nature of the perturbation added and the ocean response as it is an area of high mesoscale activity. This is illustrated by the complex evolution of the trajectories with a high temporal variability, particularly

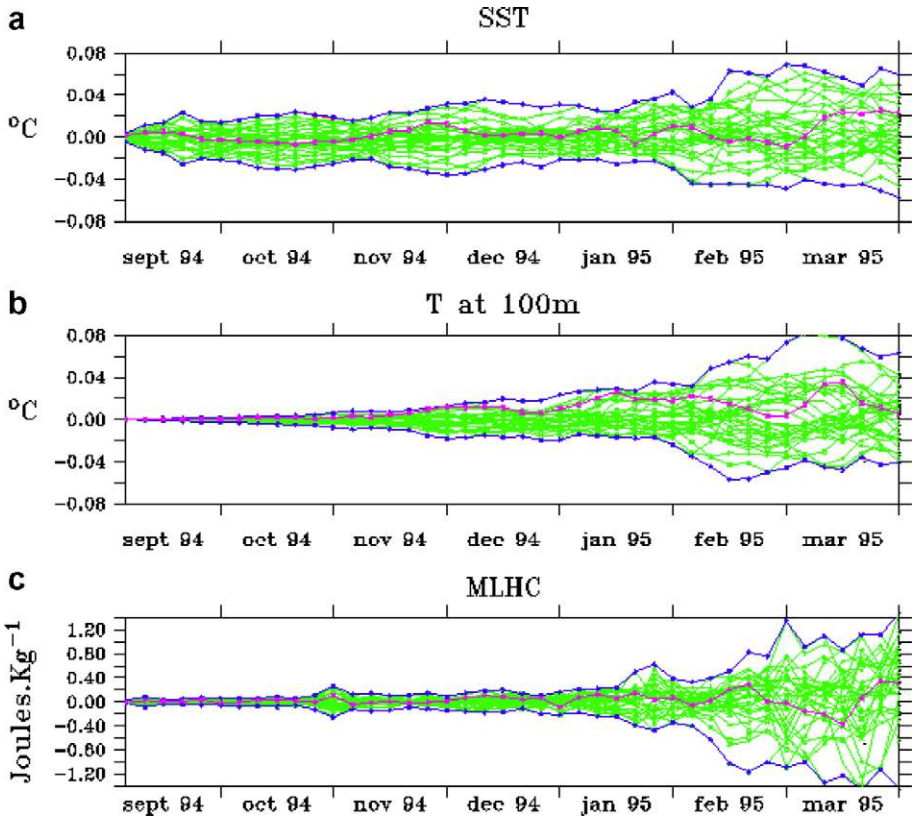

Fig. 14. Evolution as a function of time of the differences between each member's SST (panel a) temperature at 100 m (panel b) and mixed layer heat content (MLHC) (panel c) and the ensemble mean for region GS. The quantities are first averaged over the box before computing the difference with the ensemble mean. The green curves are the data for each of the first 30 members, The red curve indicates the envelope for 40 members and the blue curve, the envelope for 50 members. These often overlay the red curves. The pink curve shows the behaviour and variability of a single member.

towards the end of the experiment. At 100 m (Fig. 14b), the width of the envelope grows virtually monotonically to reach a maximum of 0.08 °C. Individually, each trajectory shows significant fluctuations in time. There is a strong coherence with what happens at the surface, probably due to the vertical coherence of the mesoscale circulation. In terms of the MLHC (Fig. 14c), it is clear that in region GS, the envelope grows virtually monotonically over time as the experiment progresses. This can be interpreted as the evidence of the progressive transmission of the signal in the vertical: over time, a greater portion of the mixed layer is perturbed which leads to an increase in the perturbation of the mixed layer heat content. In region GS, for much of the experiment, the mixed layer is deepening, dampening the effect of the temperature perturbation on the heat content, this until February where the mixed layer depth has reached a maximum. In effect, we have the same two processes described in region NEATL, the vertical transmission of the ensemble spread and the deepening of the mixed layer. Towards the end of March, the MLD starts to shallow and thus the perturbation will have relatively a greater impact on the mixed layer heat content. Because region GS is an area of high mesoscale activity, the trajectories of each member are highly non monotonic. This is particularly visible in Fig. 14c once the decorrelation of the mesoscale comes into play (mid January onwards, see below) and the envelope widens.

In region GS, the transmission in the vertical is driven by the three mechanisms discussed in the analysis of the two previous regions: diffusion, advection and mesoscale effect. The upper waters are affected by the rapid vertical diffusion which occurs in the MLD, down to about 40 m. The rate of penetration appears to weaken towards the end of the period as the mixed layer shallows and the upper waters Kz weakens (Fig. 15c),

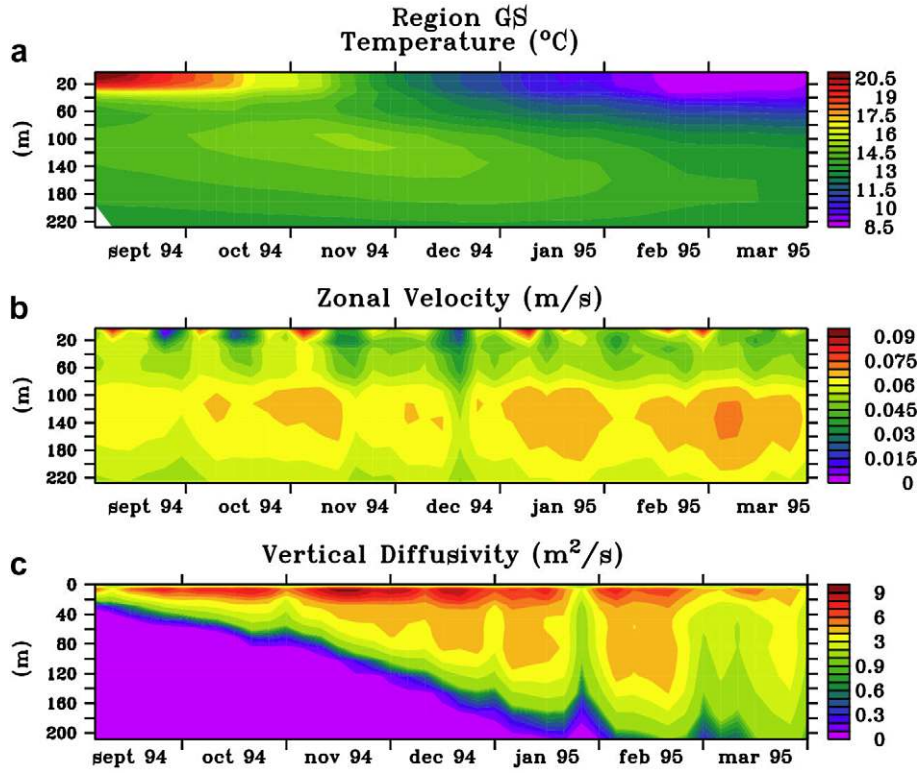

Fig. 15. Evolution as a function of time and depth of the ensemble mean temperature (°C) (panel a), mean zonal velocity (m/s) (panel b) and mean vertical diffusivity (m^2/s) (panel c) averaged over region GS.

concomitant with an increase in the spread in SST (Fig. 14a). Interestingly, Kz is never as strong in region GS as in the other regions and as a result the transmission of the atmospheric signal is never as rapid, as is illustrated by the weaker slopes in the isotherms of the temperature ensemble spread (panel c of Figs. 7, 10, and 13). At depth however, what determines the maximum in the ensemble spread of the temperature is actually the presence of a maximum in the zonal velocity field (0.9 m/s), situated at 140 m (Fig. 15b). This rapidly carries into the region the high ensemble spread of the upstream region creating a strong signal which does not get swamped by other processes. Compared to earlier occasions of high subsurface zonal velocity (October and January, Fig. 15b), the temperature ensemble spread in the upstream region which is increasing over time is much higher, leading to the strong signal observed. The large ensemble spread from the surface down to 200 m in the upstream region is the result of the eddy activity identical to what happens upstream from region TROP. It is due to the decorrelation of the mesoscale signals as suggested by the correlation plot of Fig. 16. In Fig. 16, the sea surface height (SSH) correlation of pairs of members with opposite perturbations, averaged over the ensemble is plotted for region GS and region NEATL. As the model uses the Boussinesq approximation, the SSH is purely dynamic, in other words the steric effect is not represented. It can therefore be used to track eddy signatures. Until January, the SSH correlation is virtually equal to one. This means that the paths of eddies are virtually identical in both elements of the pairs. This changes rapidly in region GS from mid January onwards where the correlation drops to 0.96, indicating that the path of eddies are starting to diverge, but not in region NEATL where, due to the absence of mesoscale activity, the correlation remains virtually equal to one throughout the experiment. These results show that, until January, the atmospheric perturbations do not induce significantly different ocean responses between the ensemble members. But, as time goes by, the non linearity of the flow tends to amplify these weak differences. It leads to the divergence of the trajectories of specific eddies or meanders between members and therefore to a time growing ensemble spread. The decorrelation time scale of the mesoscale activity due to the flow instability is thus estimated to be four months.

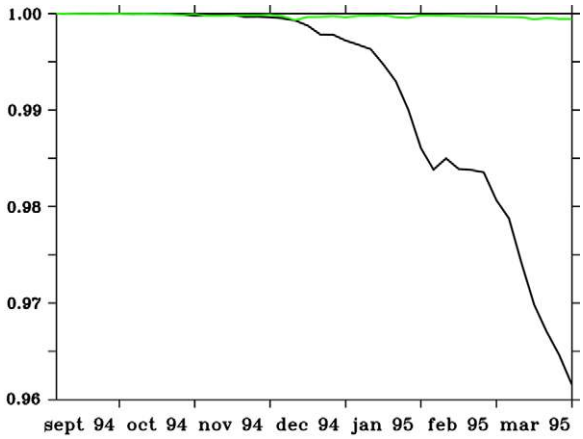

Fig. 16. Evolution of the ensemble mean of the mean zonal correlation of SSH between members pairs averaged over region GS (black line) and region NEATL (green line). For each time output (every 5 days), we start by calculating the correlation index of each zonal band in the box between two successive members perturbed by the opposite perturbation. The indices for the 50 zonal bands in a box are then averaged giving us a single index for each pair of experiments. The 25 indices are then averaged to obtain one single value per time step.

Furthermore, since the GS instabilities have a vertical coherent structure over a few hundred meters, the decorrelation of the mesoscale activity has a signature in subsurface as well.

Along with region TROP, region GS underlines the important role eddies play in generating an ocean subsurface response to the atmospheric perturbations. They have a local impact as well as a remote one through horizontal advection processes. To understand the impact of atmospheric perturbations in a given region, the origin of the waters advected is therefore crucial. For example, in region GS, the advection brings in a signal from a region of similar response to the atmospheric perturbations, i.e. upstream in the Gulf Stream. The situation is different in region TROP: the signal is advected from the North Brazil Current region, where a pronounced mesoscale activity develops in late summer and fall, into region TROP which is characterized by a weak mesoscale activity.

5. Conclusion

The aim of this study was to explore the response of the primitive equation model NATL4 to uncertainties in the atmospheric forcing fields. To this end, we use an original approach based on stochastic modelling where the atmospheric forcing fields from the ERA40 reanalysis are perturbed and an ensemble of simulations is run with the perturbed fields. The model response is then characterized from a statistical analysis over the ensemble. In this paper, we focus on the response in temperature in the upper 200 m; the study is mainly based on the analysis of the ensemble spread, its spatial distribution and time evolution. Fifty ensemble runs are made over a 7-month period corresponding to the seasonal deepening of the mixed-layer (September–March) for the years 1994–1995.

The resulting ensemble spread in temperature shows large differences in terms of spatial (including vertical) distribution and time evolution between different regions of the North Atlantic. We therefore focused our analysis on three regions characterized by different regimes: in the Gulf Stream area, in the Northern Central Tropical area and in the North East Atlantic. At the time scales of interest, we have identified three main mechanisms that are responsible for the vertical distribution of the ensemble spread in temperature: 1/vertical diffusion, 2/effect of mesoscale activity (Gulf Stream and Northern Tropical areas) and 3/horizontal advection. The vertical diffusion, acting through background diffusivity and enhanced diffusivity in case of convection, leads to a penetration of the ensemble variance from the surface to depth that is linked to the seasonal deepening of the mixed-layer. It is the main process at work in the North East Atlantic region. Mesoscale activity induces some spread in the ensemble because of the decorrelation of eddies and jet meanders between

the different runs. The depth penetration of the spread is then linked to the vertical structure of the mesoscale signals. Horizontal advection by the mean currents is essentially zonal in the areas of interest (Gulf Stream; NECC/NEUC in region TROP). It tends to advect eastward some signal created from upstream mesoscale activity. Because the currents amplitude may be subsurface intensified, advection can lead to a maximum spread in the subsurface that is decorrelated from the local surface signal. Moreover, the different time scales of the currents variability and of the mesoscale decorrelation interact, leading to complex temporal evolutions of the ensemble spread.

To our knowledge, it is the first time that a model response to atmospheric uncertainties at basin scale, over several months and in a realistic configuration is estimated. The results show the complexity of the oceanic response and illustrate the richness of the method. In particular, they underline the degree of non-stationarity and non-homogeneity of oceanic perturbations – as already clearly demonstrated in coastal models (e.g. Auclair et al., 2003; Jordà-Sanchez, 2005). However, the ocean response space–time structures in terms of temperature may be partly predictable, for example in regions of mesoscale activity, knowing the main characteristics of the mesoscale and mean circulation. It is also the case in the North East Atlantic where the spread in temperature follows the mixed-layer evolution. This study underlines as well the difficulties in deducing uncertainties on air–sea fluxes from uncertainties on atmospheric variables, because of the ocean feedback and of the non-linearity of the bulk formulae. For example, in the Gulf Stream area, heat flux and SST perturbations show a correlated monotonic increase, with initial perturbations on heat flux being intensified by the oceanic feedback. On the contrary, in the North East Atlantic area, atmospheric perturbations seem to be partially dampened; this might be due to our specific choice of perturbations but it makes difficult the prediction of their impact on air–sea fluxes locally.

We believe that most of these mechanisms (advection, diffusion, effect of mesoscale signal) are also at play when perturbing the initial conditions. In particular, the decorrelation of eddies signal can explain the divergence between the ensemble runs several weeks or months after applying the perturbation. We cannot however extrapolate the results obtained here to the impact of changes in initial conditions. It is obviously very difficult to compare the amplitude of the model response to perturbations on initial conditions (e.g. initial temperature and salinity fields) and to atmospheric forcing since we cannot compare the perturbations (amplitude, space–time structure) themselves. Furthermore, it is highly likely that perturbations in the initial conditions would modify the dynamic structure and sensitivity of the oceanic circulation elements and hence the decorrelation time scale of the system.

This study is a first step towards the estimation of model uncertainties due to atmospheric forcing fields uncertainties. A full estimation should include the analysis of the induced oceanic perturbations distribution with covariance calculations; these latter will be presented in a future paper. We believe however that the study of the ensemble variance as done here provides useful information to modelers and OGCM simulation users. The implications for modelling are many fold. In the first place, it shows that small changes in the forcing variables (often less than 1% of the reference variables amplitude, see Section 4.2) can lead to significant differences in the ocean solutions when one exceeds the decorrelation time scale of the mesoscale. It provides a kind of error bar on the solution that may help to interpret model–data misfits. It is obviously an underestimation of error bars though since other sources of model uncertainties, such as errors on initial conditions, parameters, etc., should be taken into account. When extrapolated, these results suggest that the use of two atmospheric products (e.g. ERA40 and CORE) would lead to substantial differences in the simulations. They also lead to interesting speculations on the impact of the climatological restoring, however weak, used in many runs, particularly as most climatologies have a fairly coarse resolution (monthly time scales, $1^\circ \times 1^\circ$). This restoring in all probabilities smothers a lot of the mesoscale variability responsible for the high sensitivity of the simulations to changes in atmospheric forcing fields. The results also underline the importance of resolution in the forcing products used. In effect, the perturbations added to the forcing amount to adding smaller temporal and spatial scales to the forcing and the resulting solution can diverge substantially from the reference unperturbed run. Furthermore, current reanalyses do not represent extreme events. Hence one could argue that adding those extreme events such as tropical storms and hurricanes could greatly modify the solution, particularly in the upper ocean. This in itself is not new but the results presented here can allow a first stab at quantifying the impact of adding extreme events to climatologies. As has been shown, the impact of the perturbations is not confined to the surface layer. In all likelihood, on longer time scale, it would reach the

deep ocean (beyond 1000 m) and eventually affect the slower thermohaline circulation. Our results are obviously model dependant. In particular, the impact of resolution is crucial as it determines the model's representation of the mesoscale activity. Furthermore, the structure of the perturbations and their amplitude play a significant role in the model's response. Alternative perturbations with greater spatial and temporal coherency would lead to a different response although the same mechanisms would be involved. Perturbations with higher amplitude might affect the dynamics and therefore the decorrelation time scale It is clear that, as long as there is no objective and realistic information on the forcing uncertainties, it remains very difficult to estimate the contribution of model errors due to atmospheric uncertainties to observed model–data discrepancies.

The exploration of the ensemble should include a more comprehensive description of the model response distribution. Besides the analysis of the covariances that would help to characterize the spatio-temporal structures of model uncertainties as well as the relationships between uncertainties on different variables (SST, sea surface elevation, mixed-layer depth), the comparison of the ensemble distribution to a normal one would show whether small atmospheric changes can lead to a different ocean state or not. Finally, the results point out the non-stationarity of the model response to atmospheric uncertainties, due in particular to the role of advection by current. The evolution of the model uncertainties as a function of oceanic and atmospheric regimes makes the prediction of uncertainties on forecasts difficult without using a stochastic approach. Moreover, it emphasizes the need of using space–time dependent model errors statistics in data assimilation experiments. Data assimilation is expected to reduce model errors. Its impact on errors due specifically to the forcing uncertainties can be made more efficient by specifying in the covariance matrices of forecast or background errors a priori information provided by stochastic modelling experiments such as ours.

Acknowledgements

Many thanks to J.-M. Molines (LEGI) and to S. Theetten (LPO, Brest) for helping us with the model configuration, to J.-M Brankart (LEGI) for the use of the SESAM tool for EOFS computation and to L. Brodeau (LEGI) for the use of his atmospheric forcing interpolation tool. This project was carried out with support from the Service Hydrographique de la Marine (SHOM), from the Centre National des Etudes Spatiales (CNES) through the OSTST/Jason project and from the Groupe Mission Mercator Coriolis (GMMC). Further support came from the Institut National des Sciences de l'Univers (INSU) and CNRS. Numerical simulations are made at the Institut du Développement des Ressources en Informatique Scientifique (IDRIS, Paris). Help and advice from the DRAKKAR project team are gratefully acknowledged. Many thanks to the two anonymous reviewers for their constructive comments.

References

Andreu-Burillo, I., Caniaux, G., Gavart, M., De Mey, P., Baraille, R., 2002. Assessing ocean model sensitivity to wind forcing uncertainties. Geophys. Res. Lett. 11, 1–9.

Auclair, F., Marsaleix, P., De Mey, P., 2003. Space–time structure and dynamics of the forecast error in a coastal circulation model of the Gulf of Lions. Dyn. Atmos. Oceans 36, 309–346.

Barnier, B., Madec, G., Penduff, T., Molines, J.M., Tréguier, A.M., Beckmann, A., Biastoch, A., Boning, C., Dengg, J., Gulev, S., Le Sommer, J., Rémy, E., Talandier, C., Theetten, S., Maltrud, M., Mc Lean, J., 2006. Impact of partial steps and momentum advection schemes in a global ocean circulation model at eddy permitting resolution. Ocean Dyn. 56 (5–6), 543–567.

Blanke, B., Delecluse, P., 1993. Variability of the tropical Atlantic ocean simulated by a general circulation model with two different mixed layer physics. J. Phys. Oceanogr. 23, 1363–1388.

Boccaletti, G., Ferrari, R., Ferreira, D., Adcroft, A., Marshall, J., 2005. The vertical structure of the oceanic heat transport. Geophys. Res. Lett. 32 (L10603), 1–5.

Brodeau, L., Penduff, T., Barnier, B., 2006. Sensitivity of DRAKKAR global simulations to two existing and a hybrid atmospheric forcing functions. In: Proceedings of the OSTST Meeting, Venice, 17–18 March 2006.

Caniaux, G., Planton, S., 1998. A 3D ocean mesoscale simulation using data from the SEMAPHORE experiment: mixed layer heat budget. J. Geophys. Res. 103 (C11), 25,081–25,099.

Echevin, V., De Mey, P., Evensen, G., 2000. Horizontal and vertical structure of the representer functions for sea surface measurements in a coastal circulation model. J. Phys. Oceanogr. 30, 2627–2635.

Evensen, G., 2003. The Ensemble Kalman Filter: theoretical formulation and practical implementation. Ocean Dyn. 53, 343–367. doi:11.1007/s10236-003-0036-10.

Ferrari, R., Boccaletti, G., 2004. Eddy mixed layer interaction in the ocean. Oceanography 17, 13–21.

Goosse, H., Fichefet, T., 1999. Importance of ice–ocean interactions for the global ocean circulation: a model study. J. Geophys. Res. 104, 23,337–23,355.
Jordà-Sanchez, G., 2005. Towards data assimilation in the Catalan continental shelf – from data analysis to optimization methods. PhD Thesis, Universidad Politècnica de Catalunya, Barcelona, 2005.
Kalnay, E., Kanamitsu, M., Kistler, R., Colins, W., Deaven, D., Gandin, L., Iredell, M., Saha, S., White, G., Woollen, J., Zhu, Y., Chelliah, M., Ebisuzaki, W., Higgins, W., Janowiak, J., Mo, K., Ropelewski, C., Leetmaa, A., Reynolds, R., Jenne, R., 1996. The NCEP/NCAR 40-year reanalysis project. Bull. Amer. Meteor. Soc. 77, 437–471.
Large, W., Yeager, S.G., 2004. Diurnal to decadal global forcing for ocean and sea-ice models: the data sets and flux climatologies. NCAR Technical Note.
Leeuwenburgh, O., 2005. Assimilation of along-track altimeter data in the Tropical Pacific region of a global OGCM ensemble. Quart. J. Roy. Meteor. Soc. doi:11.1256/qj.05.146.
Le Sommer, J., Penduff, T., Madec, G., 2006. How momentum advection schemes affect current-topography interactions: sensitivity studies in the North Atlantic 1/4° DRAKKAR model. Ocean Modell. (in revision).
Levitus, S., Boyer, T.P., Conkright, M.E., OBrien, T., Antonov, J., Stephens, C., Stathoplos, L., Johnson, D., Gelfield, R., 1998. World Ocean Database 1998, No. 18 in NOAA Atlas NESDIS, US Department of Commerce.
Madec, G., 2006. NEMO reference manual, ocean dynamics component: NEMO-OPA. Preliminary version. Note du Pole de modélisation, Institut Pierre-Simon Laplace (IPSL), France, 27, ISSN No. 1288-1619.
Noh, Y., Joo Jang, C., Yamagata, T., Chu, P.C., Kim, C.H., 2002. Simulation of more realistic upper-ocean processes from an OGCM with a New Ocean Mixed Layer Model. J. Phys. Oceanogr. 32 (6), 1284–1307.
Rudnick, D.L., Ferrari, R., 1999. Compensation of horizontal temperature and salinity gradients in the ocean mixed layer. Science 283, 526–529.
Stramma, L., Schott, F., 1996. Western equatorial circulation and exchange. In: Krauss, W. (Ed.), The Warmwatersphere of the North Atlantic Ocean. Gebrüder Borntraeger, Berlin, p. 446.
Troccoli, A., Kallberg, P., 2004. Precipitation Correction in the ERA-40 Reanalysis. ERA-40 Project Report Series.
Uppala, S.M. et al., 2005. The ERA40 re-analysis. Quart. J. Roy. Meteor. Soc. 131, 2961–3012.
Willebrand, J., Barnier, B., Böning, C., Dieterich, C., Killworth, P., LeProvost, C., Yia, J., Molines, J.-M., New, A.L., 2001. Circulation characteristics in three eddy-permitting models of the North Atlantic. Progr. Oceanogr. 48 (2-3), 123–161.
Wirth, A., Ghil, M., 2000. Error evolution in the dynamics of an ocean general circulation model. Dyn. Atmos. Oceans 32, 419–443.
Zhang, J., Steele, M., Rothrock, D.A., Lindsay, R.W., 2004. Increasing exchanges at Greenland–Scotland Ridge and their links with the North Atlantic Oscillation and Arctic sea ice. Geophys. Res. Lett. 31, L09307. doi:10.1029/2003GL019304.